Deformation characteristics of a single bubble in immiscible fluids

Jiarui Xu[a,b], Xiaohui Zhang[a,b,*], Shan Qing[a,b], Ronghua Li[a,b], Hua Wang[a,b]

[a]*Faculty of Metallurgical and Energy Engineering, Kunming University of Science and Technology, Kunming 650093, China*

[b]*National local Joint Engineering Research Center of Energy Saving and Environmental Protection Technology in Metallurgy and Chemical Engineering Industry, Kunming University of Science and Technology, Kunming 650093, China*

Abstract: In order to investigate characteristics of bubble deformation in immiscible fluids, the bubble shape change during the interface and the relationship between aspect ratio(E) and dimensionless number of forces is obtained. A three-dimensional model is established and the free-floating behavior of a single bubble in immiscible fluids is numerically simulated by phase-field method. The simulation results are in good agreement with experimental results. The research shows that, in the lower liquid, the relationship between E and *We*, *Ta*, *Re* is distributed between two intersecting lines. In the upper liquid, the relationship between E and *We*, *Ta*, *Re* is distributed between two parallel lines. Comparing the bubble deformation and the influence of the forces. Compared with gravity, the inertial force plays a leading role in the bubble shape in the lower liquid and upper liquid. Compared with the viscous force, the surface tension dominates the bubble shape in the lower liquid.

Key Words: Bubble shape; Immiscible liquids; Dimensionless parameter; Phase-field method.

1. Introduction

The gas-liquid multiphase flow is encountered in nuclear reactor [1], chemical [2] and metallurgical engineering [3]. Bubble motion characteristics are important in the gas-liquid flow, which closely relate to the heat and mass transfer and reaction rates. Bubble shape is a key factor of the motion characteristics. A lot of work had been carried out to study the bubble shape in a single liquid rather than immiscible liquids [4-7]. In many practical industrial processes [8], however, the bubble is in immiscible fluids.

The bubble shape has been evaluated using the aspect ratio [4,5], distortion factor [6], roundness and convexity [7]. Distortion factor is only used to describe the change of the bubble in the longitudinal direction. Roundness and convexity are used in the deformation of the crescent-moon bubble. Most researchers described the

* Corresponding author.

E-mail: xiaohui6064@qq.com

deformation of the bubble by the aspect ratio, E, the ratio of the bubble minor axis to the major axis [4,5].

The deformation of the bubble is closely related to the forces acting on the bubble. Researches results show that the shape of the bubble is mainly affected by four forces: inertial force, viscous force, surface tension and gravity force, which can be characterized by dimensionless parameters [9-16]. Therefore, researchers considered the dimensionless number of forces when studying the shape change of the bubble.

Researches on bubble deformation by using dimensionless number of forces were many, however, these researches were mainly in a single liquid. Grace et al. [10] drawn the regime map of bubble using Reynolds number (inertial force vs viscous force, *Re*), Morton number (viscous force vs surface tension, *Mo*) and Eötvös number (gravity vs surface tension, *Eo*). Some researchers obtained the empirical correlation between E and *Re*, *We*, *Eo* [11-15]. Liu et al. [16] obtained the relationship between E and dimensionless parameters of the forces in water and glycerol aqueous solution with different viscosity, which considered the viscous force and extended the previous empirical correlations [14,15]. Aoyama et al. [17,18] considered the effect of interface tension and modified the correlations by introducing dimensionless parameter Ω ($Eo^{1.12}Re$). Tian et al. [19] and Zhou et al. [20] explored the influence of different temperatures (293-493K) and pressures (0.1-6Mpa) on bubble shape, and proposed the correlation between dimensionless parameters of the forces and E. The researches on the relationship between E and dimensionless number of the forces have been investigated from the same temperature to different temperatures and pressures in a single liquid.

Many researches performed on bubble motion in immiscible liquids are mainly concentrated in two aspects: the interface change and bubble dynamics behavior. Researchers [21-28] pointed out that the interface deformation was affected by the density of immiscible fluid, interfacial tension and bubble size.

For bubble dynamics behavior in immiscible liquids, some researchers have explored it from following aspects: bubble residence time, passing pattern (flow regime) in the interface and basic behavior (shape, velocity and trajectory). Rozario [29] and Zhao et al. [30] investigated the bubble residence time in the liquid-liquid interface and found that it was closely related to the viscosity of the two fluids, especially the viscosity of the upper fluid. Researchers studied the bubble passing pattern (flow regime) in the interface, which were mainly bounce, collapse and trapped [31-36]. Some researchers obtained the basic bubble behavior in immiscible liquids. Peter et al. [37] and Bonhomme et al. [33] obtained the change of the bubble shape near the interface. Peter et al. found a transient concavity in the bottom of the bubble when it closed to the interface. Bonhomme et al. [33] classified the bubble shape before the interface using the dimensionless Bond number (buoyancy vs surface

tension, *Bo*), and Archimedes number (buoyancy vs viscous force, *Ar*). Mao et al. [38] carried out the experiment in water-mineral oil immiscible fluids, the velocity, shape and trajectory of the bubble moving from water to oil were obtained. They found that the shape and velocity of the bubble between the interface changed drastically.

The bubble deformation is greatly affected by its forces. These forces acting on the bubble can be characterized by the dimensionless numbers of forces. Researchers got the relationship between E and dimensionless numbers in a single liquid. Although the change of the bubble shape has been obtained in immiscible liquids, the relationship between the deformation and the dimensionless numbers of forces has not been reported. The bubble deformation using dimensionless numbers of forces is investigated in immiscible liquids.

The structure of this paper is as follows: the second part is the establishment and verification of the model. The third part is the results and discussion. The conclusion is presented in the fourth part.

2. Model establishment and validation

2.1. Establishment of physical model

A three-dimensional model is established in Fig. 1. Three different total fluid heights (45mm, 70mm and 100mm) are set respectively. The width of the model is set to 10 times the diameter of the bubble to eliminate the wall effect [32]. The heights of the upper (H_1) and lower layers of liquid (H_2) are shown in Fig. 2. and Table1, boundary conditions is shown in Fig. 2. According to the density difference of the two fluids, they are divided into the lower liquid and the upper liquid, the physical properties are shown in Table 2. The initial radius of the bubble is 2mm, 2.5mm, 3mm and 3.5mm respectively, and the initial height of bubble center is 5mm.

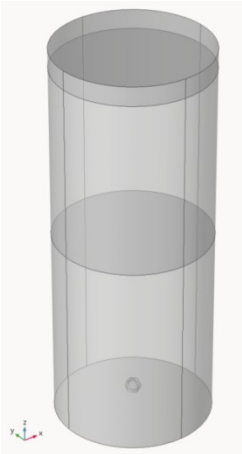

Fig. 1. Computational domain diagram

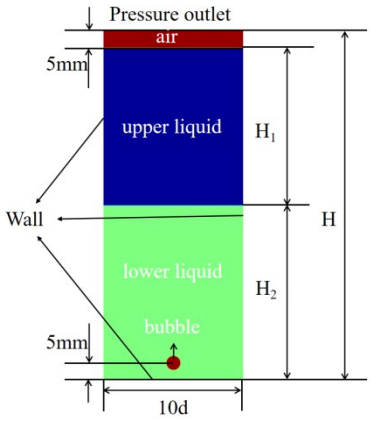

Fig. 2. Schematic diagram of physical model

Table 1. Fluid heights of three group with different total heights

Total height of fluid (H, mm)	Height of lower fluid (H_2, mm)	Height of upper fluid (H_1, mm)
45	25	15
70	45	20
100	50	45

Table 2. Physical properties of materials.

Fluid	Viscosity (Pa·s)	Density (kg·m^{-3})	Surface tension coefficient (N·m^{-1})
Lower liquid	1.003×10^{-3}	997.2	0.0727
air	2.593×10^{-5}	1.205	
Upper liquid	4.6×10^{-3}	882.4	0.0321

2.2. Establishment of mathematical model

The fluid dynamics is calculated by the Navier-Stokes equation with surface tension force [39], as shown in equation (1).

$$\rho\left(\frac{\partial u}{\partial t}+u\cdot\nabla u\right) = -\nabla p+\nabla\left[\eta\left(\nabla u+\nabla u^{t}\right)\right]+SF+\rho g \tag{1}$$

$$\nabla u = 0$$

Where ρ is the density of the fluid, kg/m3; u is the velocity of the fluid, m/s; p is the pressure, Pa; η is the viscosity of the fluid, SF is the surface tension of the interface, N.

The density and viscosity are constant in a single fluid, and the Navier-Stokes equation does not contain the surface tension term, but it is necessary to consider the surface tension between the interfaces of different fluids. The physical parameters at the interface of the three-phase flow follow the Gibbs triangle (***GT***) [40], as shown in equation (2).

$$GT = \left\{ \left(c_1, c_2, c_3 \in R^3 \right) \middle| \sum_{i=1}^{3} c_i = 1, 0 \le c_i \le 1 \right\} \tag{2}$$

Where $\mathbf{SF}=-\sum_{i=1}^{3}\alpha\varepsilon\gamma_i\nabla\cdot(\frac{\nabla C_i}{|\nabla C_i|})|\nabla C_i|\nabla C_i$ represent a certain phase in the three-phase flow, which holds when γ_i.

The surface tension SF in the Navier-Stokes equation is given by equation (3):

$$\mathbf{SF}=-\sum_{i=1}^{3}\alpha\varepsilon\gamma_i\nabla\cdot(\frac{\nabla C_i}{|\nabla C_i|})|\nabla C_i|\nabla C_i \tag{3}$$

Where Ɛ is a positive constant. To match the surface tension of the sharp-interface model, α must satisfy equation (4). Where γ_i represents the capillary coefficient for component i, $\gamma_i=\sigma_{ij}+\sigma_{ik}-\sigma_{jk}(i,j,k=1,2,3)$, and σ_{ij} represents the interface tension coefficient between the i and j fluids.

$$\int_{-\infty}^{\infty}\alpha\varepsilon\left|\nabla C_1^{eq}(x,y)\right|^2 dx=1 \tag{4}$$

Where $C_1^{eq}(x,y)=[1+\tanh(x/(2\sqrt{2}\varepsilon))]/2$ is an equilibrium composition profile in the infinite domain.

The three-component free energy for a fluid in a domain Φ is defined by equation (5) [41,42].

$$\Re = \int_{\Phi} \left[\frac{12}{\xi} E + \frac{3}{8} \xi \gamma_1 |\nabla C_1|^2 + \frac{3}{8} \xi \gamma_2 |\nabla C_2|^2 + \frac{3}{8} \xi \gamma_3 |\nabla C_3|^2 \right] d\Phi \tag{5}$$

Where $\boldsymbol{E_n}$ is the bulk free energy and shown in equation(6), ξ is the interface thickness, and is assumed to be the same among all components, $\boldsymbol{C}_i$ is given by the Cahn-Hilliard equation, which is shown in equations (7) and (8) [41,42].

$$E_n = \sigma_{12} C_1^2 C_2^2 + \sigma_{13} C_1^2 C_3^2 + \sigma_{23} C_2^2 C_3^2 + C_1 C_2 C_3 (\gamma_1 + \gamma_2 + \gamma_3) + \Lambda C_1^2 C_2^2 C_3^2 \tag{6}$$

Where Λ is a constant that is nonzero for total spreading. The spreading parameter for component i is defined as $S_i = -\gamma_i$ in ternary systems, which classifies the system to as total spreading or partial spreading. The system is to be total spreading when Si is positive for at least one component and the system is to be partial spreading when Si is negative for all components.

$$\frac{\partial C_i}{\partial t} + \nabla \cdot (u C_i) = \nabla \cdot (M_i \nabla \mu_i), i = 1,2,3 \tag{7}$$

$$\mu_i = \frac{4\gamma_T}{\xi} \sum_{j \neq i} \left[\frac{1}{\gamma_j} \left(\frac{\partial E}{\partial C_i} - \frac{\partial E}{\partial C_j} \right) \right] - \frac{3}{4} \xi \gamma_i \nabla^2 C_i, i = 1,2,3 \tag{8}$$

Where u is the macroscopic velocity, and $M_i = \frac{M_0}{\gamma_i}$ is the mobility with M_0 being an auxiliary parameter, and μ_i is the chemical potential of component i that is defined by equation(8) and where $\frac{3}{\gamma_T} = \left(\frac{1}{\gamma_1} + \frac{1}{\gamma_2} + \frac{1}{\gamma_3} \right)$ [41,42].

2.3. Grid independence verification

Fig. 3 is a grid independence verification in the condition of 2mm bubble radius and 100mm fluid height, the cells are listed in Table 3. As shown in Fig. 3, with the increase of the maximum cell size, the bubble velocity decreases. Among the

conditions for grid A, B, C, D, grid A has the highest accuracy, but the calculation cost is also highest. Considering the calculation cost and grid quality, grid B is selected.

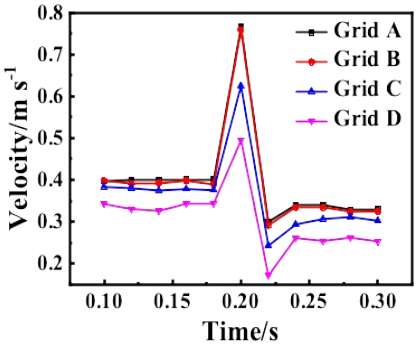

Fig. 3. Rising velocity of bubble with different mesh sizes

Table 3. Grid schemes investigation.

	Maximum cell size (mm)	Number of nodes
Grid A	0.13	1272192
Grid B	0.15	954487
Grid C	0.18	665991
Grid D	0.20	534772

2.4. Model validation

Mao et al. [38] studied the movement of bubbles with different sizes in water-oil immiscible fluids through experiments. In order to ensure the accuracy of present simulation, the experiment results of reference[38] are compared to the simulation results, which is shown in Fig. 4. The simulation conditions are set according to the experimental conditions of reference[38] (Table 4). The black and red points are the positions of the bubble at different times. The slope of line represents the velocity of the bubble. According to the comparison between the phase field model and the experimental results, therefore the phase-field model can be used to simulate bubble motion in immiscible fluids.

Table 4. Experimental conditions of reference[38]

	Reference [38]	Simulation
The total height of the bubble movement (mm)	160	160
Initial bubble equivalent diameter(mm)	5.251	5.2

The height of the lower liquid(mm)	44	44

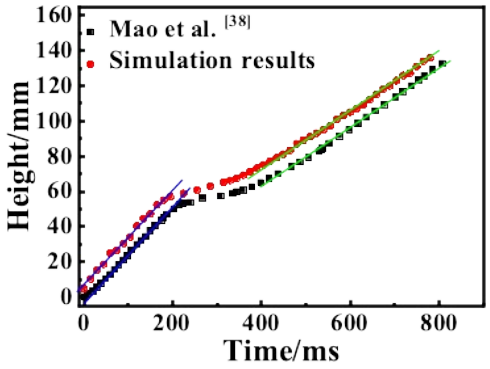

Fig. 4. Comparison between the simulation results and reference[38]

3. Results and discussion

3.1 Description of dimensionless numbers

The relationship between a single dimensionless parameter or a combination of dimensionless parameters and E (Fig. 5) is used to describe the effect of bubble forces on bubble deformation [14-19]. The physical meanings of the dimensionless numbers of the forces and the dimensionless number of the shape change are shown in equations (9)-(16) [17-19].

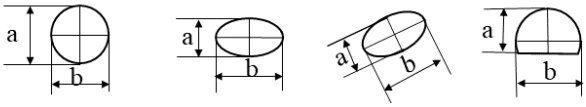

Fig. 5. Schematic diagram of E

$$Eo=\frac{g(\rho_l-\rho_g)d_{eq}^2}{\sigma_l}=\frac{F_g}{F_\sigma} \tag{9}$$

$$Mo=\frac{g\mu_l^4(\rho_l-\rho_g)}{\rho_l^2\sigma_{l^3}}=\frac{F_\mu}{F_\sigma} \tag{10}$$

$$\Re=\frac{\rho_l u d_{eq}}{\mu_l}=\frac{F_i}{F_\mu} \tag{11}$$

$$\mathbf{We}=\frac{\rho_l u^2 d_{eq}}{\sigma_l}=\frac{F_i}{F_\sigma} \tag{12}$$

$$Ga=\frac{\rho_l g(gR_{eq})^{1/2}}{\mu_l}=\frac{F_g}{F_\mu} \tag{13}$$

$$Ta=\mathrm{Re}\cdot Mo^{0.23}=\frac{F_i}{F_\mu^{0.77}F_\sigma^{0.23}}=\frac{F_i}{F_\mu}\cdot\left(\frac{F_\mu}{F_\sigma}\right)^{0.23} \tag{14}$$

$$\Omega=Eo^{1.12}\mathrm{Re}=\frac{F_g^{1.12}F_i^{1.00}}{F_\sigma^{1.12}F_\mu^{1.00}} \tag{15}$$

$$E=\frac{a}{b} \tag{16}$$

Where g is gravity acceleration, ρ_l and ρ_g are densities of fluid and gas respectively. σ_l and μ_l are the surface tension coefficient and viscosity of fluid respectively. u is the bubble velocity. d_{eq} is the equivalent diameter of the bubble, $deq = 2 * \sqrt{\pi s}$ (s is the area of the horizontal section of a bubble), $R_{eq}=1/2d_{eq}$. F_g, F_σ, F_μ and F_i are the gravity, surface tension, viscous force and inertial force on the bubble, respectively.

3.2 The bubble shape in different heights

Because of the different physical parameters of lower and upper liquid, the bubble shape changes dramatically when it passes through the interface. According to Fig. 6, the change of E can be divided into four stages: (I)E decreases in the lower liquid; (II)E remains stable in the lower liquid; (III)E fluctuates up and down between the interface; (IV)E remains stable in the upper liquid. Stage I and III occurred in 3 groups of heights, but stage II and IV can not be found or not so obviously in 45mm and 75mm, only when the height is 100mm, the four stages are obvious, so the subsequent studies are based on the height of 100mm.

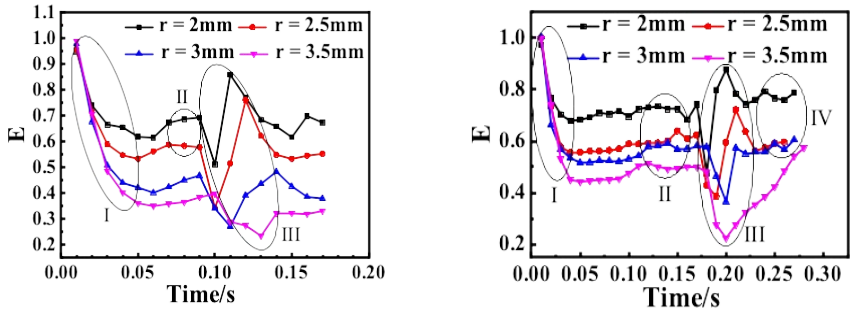

(a)45mm (b)70mm

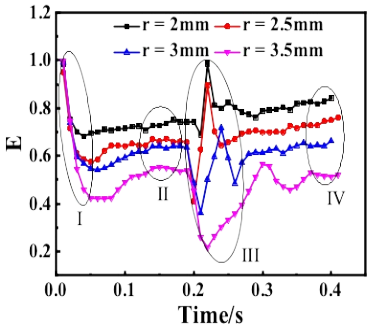

(c)100mm

Fig. 6. The change of E with time

As shown in Fig. 6(c), the bubble remains stable state both in the lower liquid and the upper one after a certain distance, and the aspect ratio at this time is called the terminal aspect ratio, E_T. According to Fig. 7, with the increase of bubble diameter, E_T decreases; E_T in the lower liquid is smaller than in the upper, but with the diameter increase, the difference of E_T becomes smaller. The reason is that the upper liquid has a larger viscous force. It is easier for the same size bubble to maintain a spherical shape with a larger viscous force. The smaller bubble is easier to maintain the spherical shape because of the greater surface tension on it, so the smaller bubble has a larger aspect ratio in upper liquid.

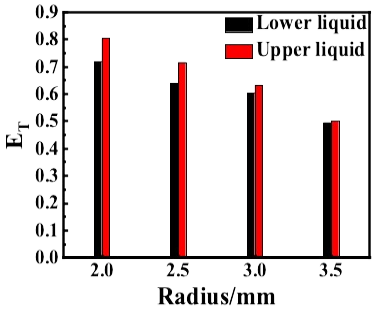

Fig. 7. E_T of different radius bubble

The shape of the bubble changes violently when it passes through the interface. To obtain the shape change of the bubble in the interface, E is taken every 0.001s of movement when crossing the interface. Fig. 8 shows the change of E when the bubble passes through the interface in 100mm. In this process, E first decreases and then increases, and the decreasing time is shorter than increasing time, and with the increase of bubble size, the time difference becomes more obvious. It takes longer for E from small to large with the increase of bubble radius, because the wake vortex formed by the lower liquid at the bottom of the bubble inhibits bubble movement, and the larger the bubble is, the stronger the wake vortex is (Fig. 9). E is closer to 1 when

the bubble is about to exit the interface than when it just contacts the interface. The reason is that the inertia force is weakened when the bubble just contacts the interface, and then the viscous force of the bubble is strengthened, but increases slowly.

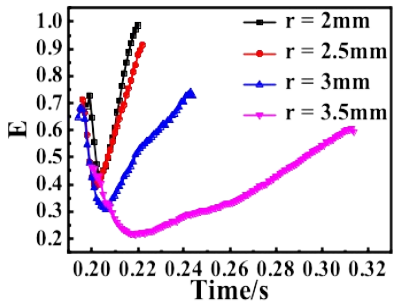

Fig. 8. Changes of aspect ratio when crossing the interface

As shown in Fig. 9, the vortex distribution map of the bubble passing through the interface is shown. According to Fig. 8, E first decreases and then increases when the bubble crosses the interface, take a moment in the decreasing time period and increasing time period respectively, and then draw the vortex distribution, the red represents the bubble, the blue represents the lower liquid, the green represents the upper liquid and the solid line represents the velocity isoline. The bubble with a radius of 2 and 2.5mm has obvious internal vortices. The bubble with a radius of 3 and 3.5mm form a tail vortex, and the strength of the tail vortex increases as the bubble radius increases. The maximum wake vortex intensity of a bubble with a radius of 3mm is 0.3277m/s at 0.223s, and a bubble with a radius of 3.5mm is 0.3439m/s at 0.245s. The wake vortex causes the bubble to stay in the interface for a longer time.

R=2mm

0.201s

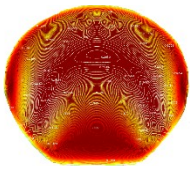

0.215s

R=2.5mm

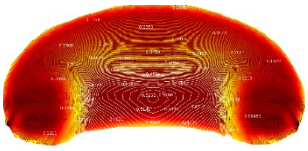

0.201s

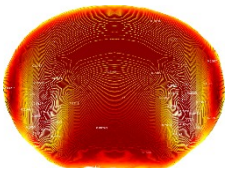

0.215s

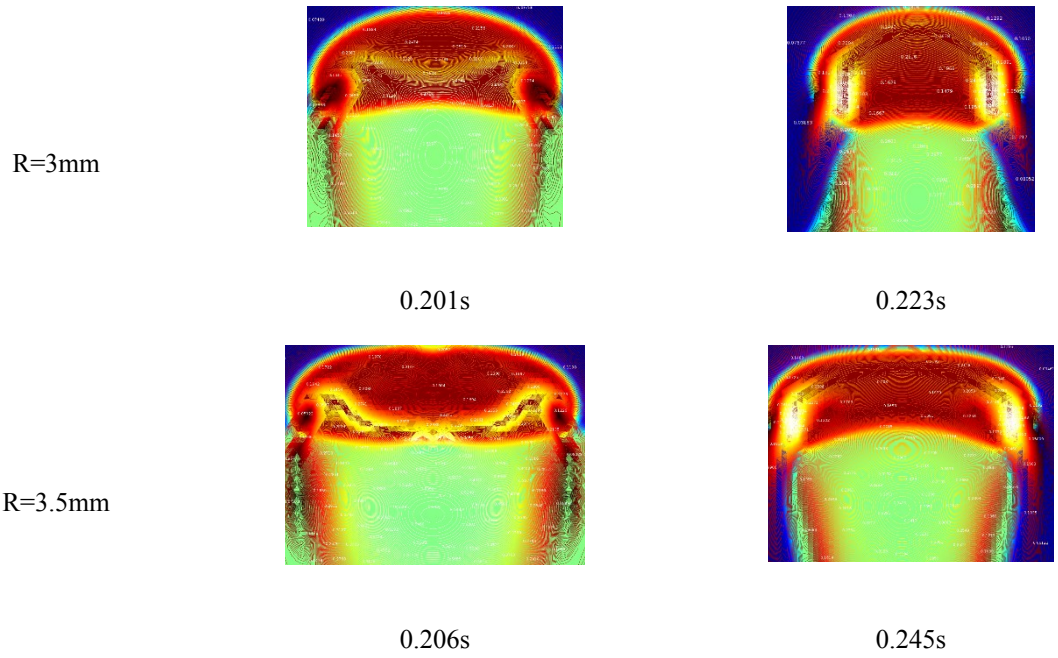

Fig. 9. The bubble vortex distribution map in the interface

Fig. 10 is the profile of a bubble with a radius of 3mm passing through the interface. During the whole process from the bubble contacting the interface to leaving the interface, the shape of the bubble with different radius is mainly divided into the following four shapes: “pear” shape(a), inverted “pear” shape(b), “convex” shape(c), and “droplet” shape(d). Combined with the change of E in Fig. 8, the pear-shape and inverted pear-shape bubbles have larger aspect ratios, the convex-shape bubble has smaller aspect ratios, and the drop-shape bubble has the largest aspect ratio. Therefore, it takes the shortest time for the bubble to deform from “pear” shape to inverted “pear” shape, and the longest time to keep “convex” shape.

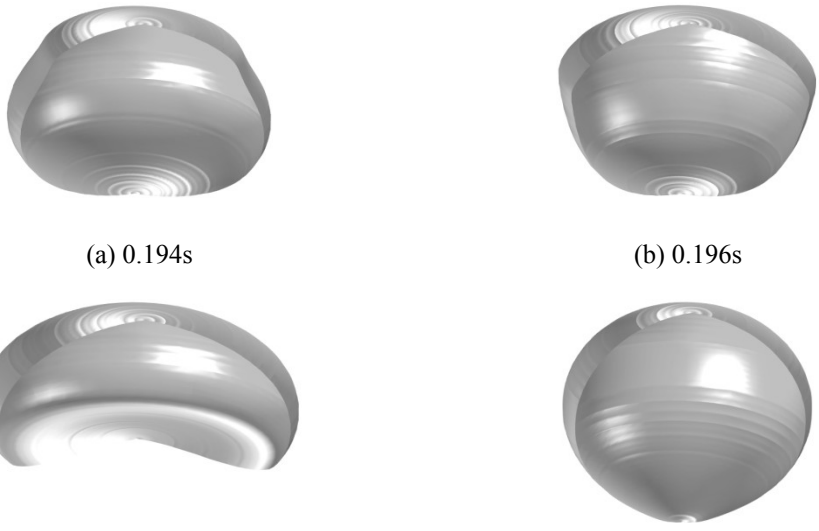

(a) 0.194s

(b) 0.196s

(c) 0.216s

(d) 0.240s

Fig. 10. The profile of the bubble when crossing interface(R=3mm)

3.3 Relationship between E and *We*, *Ta*, *Re*, Ω, *Eo*, *Ga*

The bubble shape is extremely unstable during the rising process because of the existence of the interface. The following is the relationship between instantaneous bubble aspect ratio and dimensionless numbers of the forces in the total fluid height of 100mm. The values of *Ta*, *Eo*, *Mo*, *Re*, *Ga*, Ω and E are obtained for every 0.01s.

3.3.1 In the lower liquid

Fig. 11 is the result of the bubble from the initial position to the liquid-liquid interface. (a), (b), (c), (d), (e) and (f) represent the relationship between E and *We*, *Ta*, *Re*, Ω, *Eo*, *Ga*, respectively. The results of the different radius bubbles have different distribution areas. As the bubble radius increases, *We*, *Ta*, *Re*, Ω, *Eo* and *Ga* increase while E decreases.

The relationship between E and *We*, *Ta*, *Re* is distributed between two intersecting lines. The relationship between E and *We*: it is distributed between two straight lines with slopes of -0.0726 and -0.0207. The relationship between E and *Ta*: it is distributed between two straight lines with slopes of -0.1007 and -0.0362. The relationship between E and *Re*: it is distributed between two straight lines with slopes of -4.459×10^{-4} and -1.325×10^{-4}.

The relationship between E and Ω, *Eo*, *Ga* is more concentrated and distributed near a straight line. The relationship between E and Ω: it is distributed near the straight line with slope of -3.325×10^{-5}, the maximum range is +65.49%, the minimum range is -41.31%. The relationship between E and *Eo*: it is distributed near the straight line with slope of -0.0855, the maximum range is +33.12%, the minimum range is -38.36%. The relationship between E and *Ga*: it is distributed near the straight line with slope of -8.73×10^{-4}, the maximum range is +29.62%, the minimum range is -40.89%.

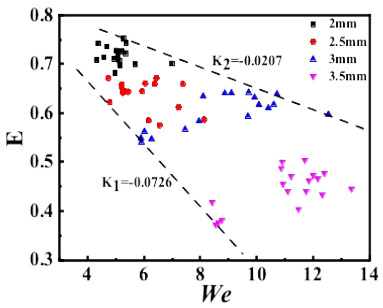

(a)

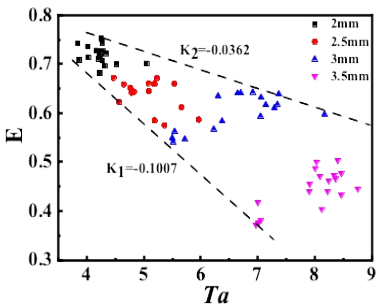

(b)

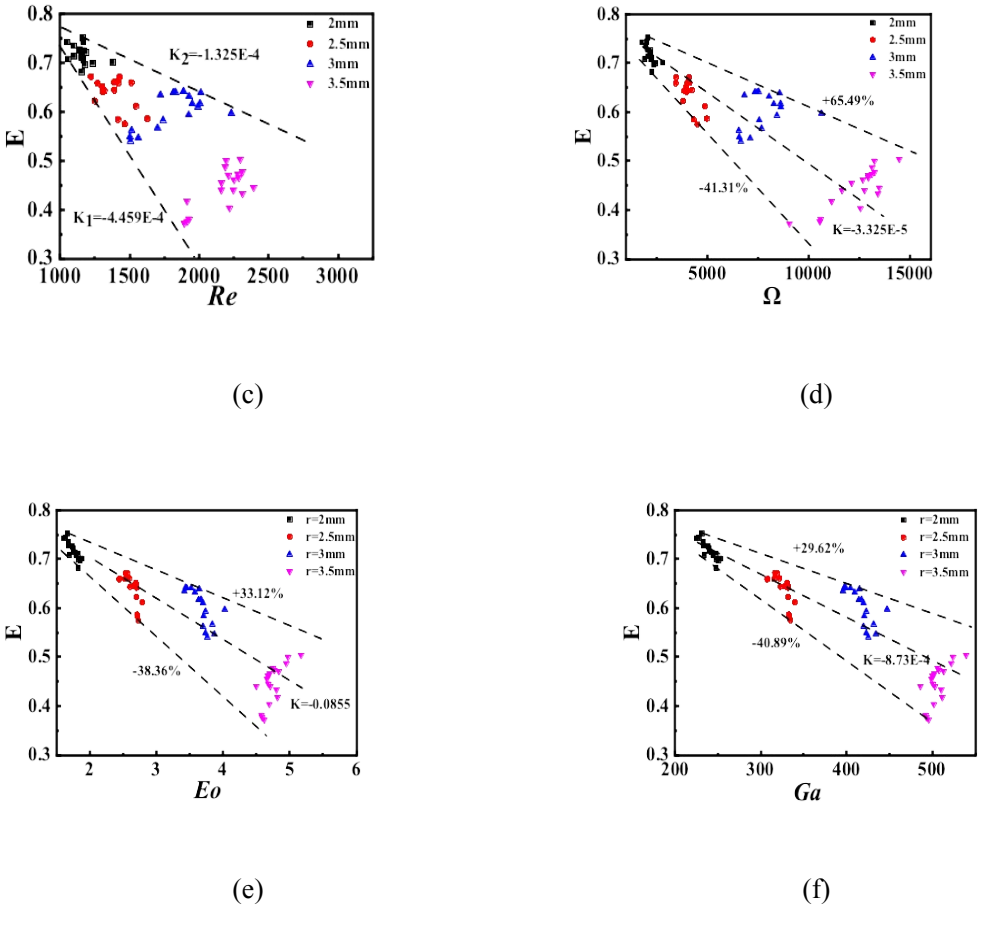

(c) (d)

(e) (f)

Fig. 11. Relationship between E and *We*, *Ta*, *Re*, Ω, *Eo*, *Ga* in the lower liquid

3.3.2 In the upper fluid

The bubble continues to rise in the upper liquid after fully crossing the interface. Fig. 12 are the results of the bubble from the liquid-liquid interface to the liquid-gas interface. (a), (b), (c), (d), (e) and (f) represent the relationship between E and *We*, *Ta*, *Re*, Ω, *Eo*, *Ga* in the upper liquid, respectively. As the bubble radius increases, *We*, *Ta*, *Re*, Ω, *Eo* and *Ga* increase while E decreases.

The relationship between E and *We*, *Ta*, *Re* is zonal distributed and distributed between two parallel lines. The relationship between E and *Re*: it is distributed between two straight lines with slopes of -2.6729×10^{-3}. The relationship between E and *Ta*: it is distributed between two straight lines with slopes of -0.1112. The relationship between E and *We*: it is distributed between two straight lines with slopes of -0.0613. Compared with (a), (b) and (c) in Fig. 11, the distribution of smaller bubbles is more concentrated in lower liquid. However, the concentration of data obtained in upper liquids is not directly related to initial bubble size.

The relationship between E and Ω, *Eo*, *Ga* is linear distributed and closely distributed near a certain straight line. The relationship between E and Ω: it is

distributed near the straight line with slope of -1.394×10^{-4}, the maximum range is +10.54%, the minimum range is -41.96%. The relationship between E and *Eo*: it is distributed near the straight line with slope of -0.0826, the maximum range is +32.69%, the minimum range is -14.77%. The relationship between E and *Ga*: it is distributed near the straight line with slope of -6.993×10^{-3}, the maximum range is +10.14%, the minimum range is -12.58%. From (a), (b), (c) to (d), (e), (f), it is from scattered zonal distribution to concentrated linear distribution. Compared with (d), (e) and (f) in Fig. 11, the relationship between E and Ω, *Eo*, *Ga* is linear distributed both the upper liquid and the lower liquid, while the distribution is more concentrated in upper liquid.

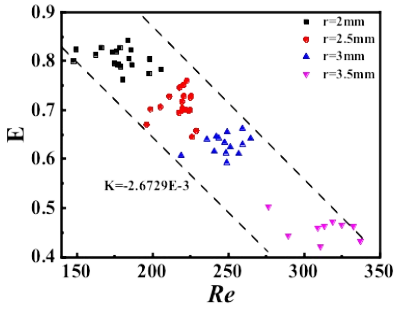

(a)

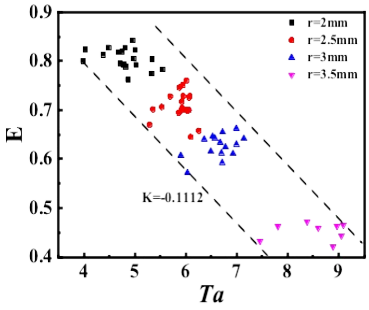

(b)

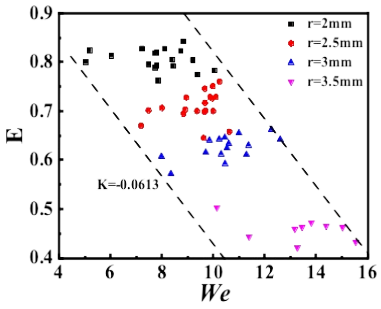

(c)

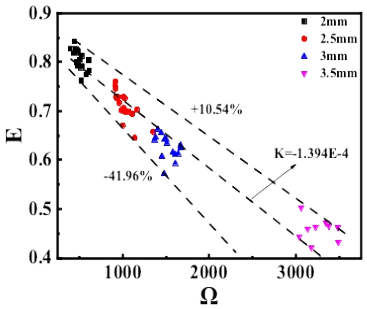

(d)

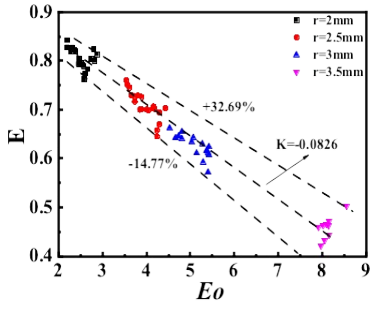

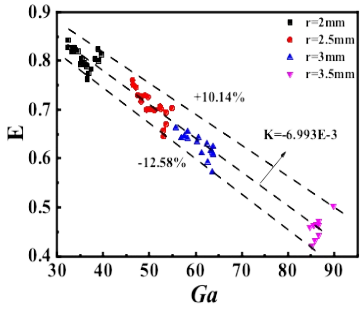

(e) (f)

Fig. 12. Relationship between E and *Re*, *Ta*, *We*, Ω, *Eo*, *Ga* in the upper liquid

3.4 The relationship between *Ga* and *Re*, *Eo*

The deformation of the bubble is closely related to the forces acting on the bubble [9-16]. Fig. 13 (a) and (b) show the relationship between *Ga* and *Re* every 0.01s in the lower liquid and upper liquid respectively. *Re* and *Ga* of different radius bubbles are distributed in different areas. With the increase of bubble radius, *Re* and *Ga* increase. The values in Table 5 are the change rates of *Ga*, *Re*, *Eo* and E. According to Table 5, the change rate of E is larger in lower liquid than the upper liquid, and the change rate of Re is larger than *Ga* both lower and upper liquid. Therefore the inertial force plays a leading role in the bubble shape in the lower liquid. The change rate of *Re* decreases and the change rate of *Ga* increases as the bubble moves from the lower liquid to the upper liquid. The change rate of E decreases in this process. So, the inertial force plays a leading role in the bubble shape both in the lower liquid and the upper one.

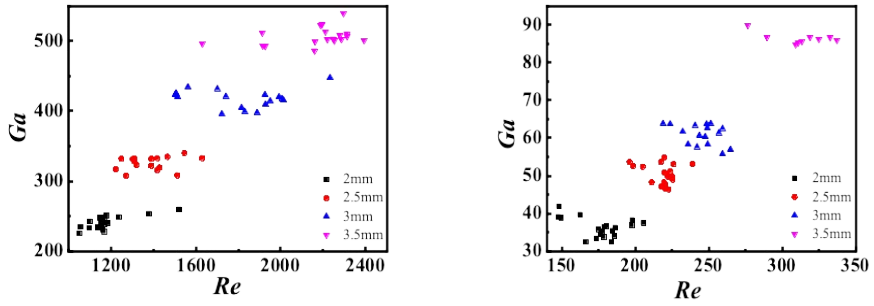

(a) (b)

Fig. 13. Relationship between Ga and Re

(a) lower liquid (b) upper liquid

Table 5. The variation ranges of *Ga*, *Re*, *Eo* and E

Radius	$\frac{\Re_{max}-\mathrm{Re}_{min}}{\mathrm{Re}_{min}}$		$\frac{Ga_{max}-Ga_{min}}{Ga_{min}}$		$\frac{Eo_{max}-Eo_{min}}{Eo_{min}}$		$\frac{E_{max}-E_{min}}{E_{min}}$	
(mm)	lower liquid	upper liquid	lower liquid	upper liquid	lower liquid	upper liquid	lower liquid	upper liquid
2	0.4501	0.3916	0.1508	0.2916	0.2060	0.4066	0.4451	0.0677
2.5	0.3333	0.3112	0.0884	0.1841	0.1195	0.2527	0.6511	0.1783

3	0.4863	0.1851	0.1301	0.1447	0.1771	0.1975	0.8367	0.2039
3.5	0.4084	0.2196	0.1097	0.0599	0.1489	0.0807	1.3739	0.2358

In Fig. 14, with the increase of bubble size, *Eo* and *Ga* both increase linearly in the lower liquid and upper liquid. There are the change rates of *Ga*, *Eo* and E in Table 5. According to Table 5, the change rate of *Eo* is larger than *Ga* in lower liquid, and the change rate of E is larger in lower liquid. Therefore compared with the viscous force, the surface tension plays a leading role in the bubble shape in the lower liquid.

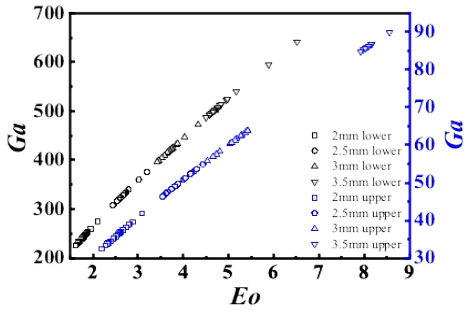

Fig. 14. Relationship between *Ga* and *Eo*

4. Conclusions

Deformation characteristics of a single bubble in immiscible liquids is investigated. Shape change of the bubble in the liquid-liquid interface and the relationship between the instantaneous deformation of the bubble and the dimensionless number of forces in lower and upper liquid is analyzed. Several conclusions can be drawn as follows:

(1) E will remain stable after fluctuating for some distance both in the lower liquid and the upper one when the height of the lower and upper fluid is appropriate. When the bubble passes through the interface, E decreases first and then increases, and the decreasing time is shorter than increasing time.

(2) In the interface, the shape of the bubble with different radius is divided into four shapes in turn: “pear” shape, inverted “pear” shape, “convex” shape, and “droplet” shape.

(3) In lower liquid, the relationship between E and *We*, *Ta*, *Re* is decentralized distribution with different radius bubble. However, the relationship between E and Ω, *Eo, Ga* is centralized distribution. The relationship between E and *We*, *Ta*, *Re* is without clear distribution boundaries and is distributed between two intersecting lines. The relationship between E and Ω, *Eo*, *Ga*: it is distributed near the slope of the line with -3.325×10^{-5}, -0.0855, and -8.73×10^{-4}, respectively.

(4) In upper liquid, the relationship between E and *We*, *Ta*, *Re* is distributed between

two parallel lines. The relationship between E and Ω, *Eo*, *Ga* is similar to lower liquid and distributed near the slope of the line with -1.394×10^{-4}, -0.0826 and -6.993×10^{-3}. While, the distribution is more concentrated in upper liquid.

(5) Compared with gravity, the inertial force plays a leading role in the bubble shape in the lower liquid and upper liquid. Compared with the viscous force, the surface tension dominates the bubble shape in the lower liquid.

Acknowledgement

The research is supported by National Natural Science Foundation of China (No. 51966005) and Science Research Foundation of Yunnan Education Bureau (No. 2019J0033).

Reference

[1] Saraswat S. P., Munshi P., Allison C., Linear stability analysis of RELAP5 two-fluid model in Nuclear Reactor Safety Results. *Annals of Nuclear Energy*, 2020, 149.

[2] Kalmár C., Klapcsik K., Hegeds F., Relationship between the radial dynamics and the chemical production of a harmonically driven spherical bubble. *Ultrasonics Sonochemistry*, 2020, 64.

[3] Hallet V., Belie D. B., Pontikes Y., The impact of slag fineness on the reactivity of blended cements with high-volume non-ferrous metallurgy slag. *Construction and Building Materials*, 2020, 257.

[4] Tomiyama A., Drag, lift and virtual mass forces acting on a single bubble. *International Symposium on Two-Phase Flow Modelling and Experimentation*, 2004.

[5] Rastello M., Marié, Louis J., Lance M., Drag and lift forces on clean spherical and ellipsoidal bubbles in a solid-body rotating flow. *Journal of Fluid Mechanics*, 2011, 682:434-459.

[6] Myint W., Hosokawa S., Tomiyama A., Shapes of Single Drops Rising Through Stagnant Liquids. *Journal of Fluid Science and Technology*,2007, 2(1):184-195.

[7] Hallmark B, Chen C. H., Davidson J. F., Experimental and simulation studies of the shape and motion of an air bubble contained in a highly viscous liquid flowing through an orifice constriction. *Chemical Engineering Science*, 2019, 206: 272-288.

[8] Wang Q., Guo X., Wang S., et al., Multiphase equilibrium modeling of oxygen bottom-blown copper smelting process. *Transactions of Nonferrous Metals Society of China*, 2017, 27(11): 2503-2511.

[9] Clift R., Grace J. R., Weber, M. E. Bubbles, drops, and particles.1978.

[10] Grace J. R., Wairegi T., Nguyen T. H., Shapes and velocities of single drops and bubbles moving freely through immiscible liquids. *Transactions of the Institution of Chemical Engineers*, 1976, 54(3): 167–173.

[11] Moore D. W., The rise of a gas bubbles in a viscous liquid, *Journal of Fluid Mechanics*, 1959, 6(1): 113-130.

[12] Tadaki T., Maeda S. On the Shape and Velocity of Single Air Bubbles Rising in Various Liquids. *Chemical Engineering*, 1961, 25(4): 254-264.

[13] Taylor T. D., Acrivos A., On the deformation and drag of a falling viscous drop at low Reynolds number.*Journal of Fluid Mechanics*,1964, 18(3): 466-476.

[14] Sugihara K., Sanada T., Shirota M., Watanabe M., Behavior of single rising bubbles in superpurified water. *Kagaku Kogaku Ronbun*, 2008, 33(5): 402-408.

[15] Legendre D., Zenit R., Velez-Cordero J. R., On the deformation of gas bubbles in liquids. *Physics of Fluids*, 2012, 24(4):113.

[16] Liu L., Yan H., Zhao G., Experimental studies on the shape and motion of air bubbles in viscous liquids. *Experimental Thermal and Fluid Science*, 2015, 62: 109–121.

[17] Aoyama S., Hayashi K., Hosokawa S., Tomiyama A., Aoyama K., Shapes of ellipsoidal bubbles in infinite stagnant liquids, *International Journal of Multiphase Flow*, 2016, 79: 23–30.

[18] Aoyama S., Hayashi K., Hosokawa S., et al., Shapes of single bubbles in infinite stagnant liquids contaminated with surfactant. *Experimental Thermal and Fluid Science*, 2018, 96: 460-469.

[19] Tian Z., Cheng Y., Li X., et al., Bubble shape and rising velocity in viscous liquids at high temperature and pressure. *Experimental Thermal and Fluid Science*, 2019, 102: 528-538.

[20] Zhou Y., Zhao C., Bo H., Analyses and modified models for bubble shape and drag coefficient covering a wide range of working conditions. *International Journal of Multiphase Flow*, 2020, 127.

[21] Greene G., Chen J., Conlin M., Onset of Entrainment Between Immiscible Liquid Layers Due to Rising Gas-Bubbles. *International Journal of Heat and Mass Transfer*, 1988, 31(6): 1309−1317.

[22] Greene G., Chen J., Conlin M., Bubble Induced Entrainment Between Stratified Liquid Layers. *International Journal of Heat and Mass Transfer*, 1991, 34(1), 149−157.

[23] Dong C., Guo K., Cai Q., et al., Simulation on mass transfer at immiscible liquid interface entrained by single bubble using particle method. *Nuclear Engineering and Technology*, 2020, 52(6): 1172-1179.

[24] Reiter G., Schwerdtfeger K., Observations of Physical Phenomena Occurring During Passage of Bubbles Through Liquid/Liquid Interfaces. *ISIJ International*, 1992, 32(1), 50−56.

[25] Reiter G., Schwerdtfeger K., Characteristics of Entrainment at Liquid-Liquid Interfaces Due to Rising Bubbles. *ISIJ International*, 1992, 32(1), 57−65.

[26] Natsui S., Takai H., Kumagai T., et al., Multiphase Particle Simulation of Gas Bubble Passing Through Liquid/Liquid Interfaces. Materials Transactions, 2014, 55(11): 1707-1715.

[27] Natsui S., Nashimoto R., Takai H., et al., SPH simulations of the behavior of the interface between two immiscible liquid stirred by the movement of a gas bubble. *Chemical Engineering Science*, 2016, 141: 342-355.

[28] Shaw J. M., Konduru R., The behaviour of large gas bubbles at a liquid-liquid interface. Part 2: Liquid entrainment. *The Canadian Journal of Chemical Engineering*, 1992.

[29] Rozario A., Viswanathan N. N., Basu S., Rise of Gas Bubbles Across the Interface Between Two Liquids. *Metallurgical and Materials Transactions B*, 2019, 50(1):10-15.

[30] Zhao H., Wang J., Zhang W., et al., Bubble Motion and Interfacial Phenomena during Bubbles Crossing Liquid–Liquid Interfaces. *Processes*, 2019, 7(10).

[31] Yin Z., Huang Z., Tu C., et al., Dynamic Characteristics of Bubble Collapse Near the Liquid-Liquid Interface. *Water*, 2020, 12(10).

[32] Xu Y., Ersson M., Jnsson P. G., Numerical Investigations on Bubble Behavior at a Steel–Slag Interface. *Steel research international*, 2020, 91(6): 1-7.

[33] Bonhomme R., Magnaudet J., Duval F., Piar B., Inertial Dynamics of Air Bubbles Crossing a Horizontal Fluid−fluid Interface. *Journal of Fluid Mechanics*, 2012, 707: 405−443.

[34] Singh K. K., Gebauer, F., Bart H. J., Bouncing of a Bubble at a Liquid-Liquid Interface. *AIChE Journal*, 2017, 63(7): 3150−3157.

[35] Emery T. S., Raghupathi P. A., Kandlikar S. G., Flow Regimes and Transition Criteria during Passage of Bubbles through a Liquid−Liquid Interface. *Langmuir*, 2018,34(23): 6766-6776.

[36] Emery T. S., Kandlikar S. G., Modeling Bubble Collisions at Liquid-Liquid and Compound Interfaces. *Langmuir*, 2019, 35(25): 8294-8307.

[37] Shopov P., Minev P., The unsteady motion of a bubble or drop towards a liquid-liquid interface. *Journal of Fluid Mechanics*, 1992, 235: 123-141.

[38] Mao N., Kang C., Teng S., Mulbah C., Formation and detachment of the enclosing water film as a bubble passes through the water-oil interface, *Colloid and Surface A.*, 2020, 586.

[39] Kim J., Phase field computations for ternary fluid flows, *Computer Methods in Applied Mechanics and Engineering*, 2007,196: 4779-4788.

[40] Ling K., Zhang S., Wu P., A coupled volume-of-fluid and level-set method (VOSET) for capturing

interface of two-phase flows in arbitrary polygon grid. *International Journal of Heat and Mass Transfer*, 2019, 143.

[41] Reza H. A., Fakhari A., Rahimian M. H., Numerical simulation of three-component multiphase flows at high density and viscosity ratios using lattice Boltzmann methods. *Physical Review E*, 2018, 97(3).

[42] Raha K., Adel E., Seyed M. H., Hong L., Three-component phase-field Lattice Boltzmann method with high densi ty ratio and ability to simulate total spreading states, *Computers and Fluids*, 2020, 204.